Available online at www.sciencedirect.com
ScienceDirect
Trans. Nonferrous Met. Soc. China 29(2019) 558−568
Transactions of Nonferrous Metals Society of China
www.tnmsc.cn

Orientation dependence of transverse tensile properties of nickel-based third generation single crystal superalloy DD9 from 760 to 1100 °C

Wan-peng YANG, Jia-rong LI, Shi-zhong LIU, Zhen-xue SHI, Jin-qian ZHAO, Xiao-guang WANG

Science and Technology on Advanced High Temperature Structural Materials Laboratory, Beijing Institute of Aeronautical Materials, Beijing 100095, China

Received 12 December 2017; accepted 2 July 2018

Abstract: At temperatures ranging from 760 to 1100 °C, the tensile properties of a nickel-based third generation single crystal superalloy DD9 with [100], [120] and [110] orientations were studied. The microstructures and fracture surfaces were observed by OM, SEM and TEM. Results show that the tensile strength of [100] specimen is higher than that of [120] and [110] specimens at 760 and 850 °C; while at the temperatures higher than 980 °C, the tensile strength of all specimens has little difference. The fracture mechanisms of [100], [120] and [110] specimens are the same at 760 and 980 °C. At 1100 °C, the fracture surfaces of [100] and [120] specimens are characterized by dimple features; while [110] specimen shows mixed quasi-cleavage and dimple featured fracture surfaces. At 760 °C, obvious superlattice stacking faults (SSFs) are observed only in [100] specimen; while at 1100 °C, the dislocation configurations of all specimens are similar. The difference in the number of potential active slip systems in [100], [120] and [110] specimens during the tensile deformation process is the main reason for the transverse tensile anisotropy.
Key words: third generation single crystal superalloy; DD9; transverse tensile properties; anisotropy; fracture surface

1 Introduction

Nickel-based single crystal superalloys are the main materials for turbine blades in advanced aero gas turbine engines due to their superior comprehensive properties [1−3]. Single crystal turbine blades in advanced aero engines have to withstand high service temperatures and stresses, and the principal stress axes is usually parallel to [001] orientation of the single crystal turbine blade. Meanwhile, the stress state in the rabbet is complex, and the rabbet would sustain tensile stress which is perpendicular to the [001] orientation. However, in most turbine blade castings, the [100] orientation, which is the direction perpendicular to the [001] orientation, is neither specified nor controlled during the manufacturing process [4]. Therefore, the [100] orientation for a given blade castings becomes a random variable.

Numerous research works have been done concerning the tensile properties of nickel-based single crystal superalloys. Most of the previous studies have focused on the [001] orientation [5−7]. The yield strength is observed to be nearly constant or increase as the temperature increases to a peak temperature and then decreases with the temperature increasing. The tensile anisotropy of single crystal superalloys has also been investigated [8−11]. It is reported that the tensile anisotropy drops as the temperature increases. Some work has been done about the effect of secondary orientation ([100] or [010] orientation) on the longitudinal tensile properties [12,13]. It was predicted that the [100] orientation optimization could be a potential way to further improve the mechanical properties of single crystal turbine blades.

Till now, there are a few studies about the transverse tensile properties of the single crystal superalloys. The transverse tensile properties of the second generation single crystal superalloy DD6 have been investigated [14,15]. However, the transverse tensile anisotropy is seldom reported in the open literature, yet this is still one of the important research aspects to assure the quality of the single crystal superalloy turbine blades. DD9 alloy is a third generation single crystal superalloy, which is developed by Beijing Institute of Aeronautical Materials (China) for advanced aero engine blade applications [2]. The primary goal of this work is to report the transverse tensile anisotropy of DD9 alloy at

Corresponding author: Wan-peng YANG; Tel: +86-10-62498312; E-mail: wp_yang621@126.com
DOI: 10.1016/S1003-6326(19)64964-2

temperatures ranging from 760 to 1100 °C. This could provide both the scientific basis and the technical support for the structural design and microstructure optimization of DD9 single crystal turbine blades.

2 Experimental

The chemical compositions of DD9 alloy are (wt.%): 3.5 Cr, 7 Co, 2 Mo, 6.5 W, 5.6 Al, 7.5 Ta, 4.5 Re, 0.1 Hf, 0.5 Nb, 0.008 C and Ni balance. The master alloy was melted in a vacuum induction furnace with commercially pure raw materials. Single crystal superalloy slabs with dimensions of 15 mm × 80 mm × 120 mm were cast in a directional solidification vacuum furnace using seed crystal method. The orientations of the single crystal slabs were determined with X-ray technology, and the slabs with [001] orientation deviating from the longitudinal direction within 10° were chosen.

The schematic of the single crystal slab and the transverse specimen is shown in Fig. 1. Three kinds of seeds were used. The longitudinal orientations of all the seeds were [001], and the transverse orientations of the seeds are [100], [120] and [110], respectively. Consequently, three kinds of transverse specimens were obtained. As seen in Fig. 1, top view A shows the transverse specimen with a regular [100] orientation, while top view B and C shows the [100] orientation deviating from the regular [100] orientation by an angle α in (001) plane. If α=26°, the transverse specimen is [120]-orientated, and the transverse specimen is [110]-orientated if α=45°. The initial transverse orientation of the specimens was then verified by the X-ray technology. The tensile axis orientations of the specimens are shown in Fig. 2. It can be seen that almost all specimens orientated near the [100]−[110] boundary. Type A specimens have transverse orientations close to the [100] pole of the standard stereographic triangle, while Type C specimens have transverse orientations close to the [110] pole. Type B specimens have transverse orientations within 20°−26° of the [100] direction. Therefore, these three kinds of transverse specimens can be denoted to be [100] specimen, [120] specimen and [110] specimen, respectively.

All specimens received a heat treatment regime as follows [2]: pre-heat treatment + (1340 °C, 6 h), AC + (1120 °C, 4 h), AC + (870 °C, 32 h), AC. Then, the specimens were machined into tensile test specimens with a gauge length of 25 mm and a diameter of 5 mm. The tensile test was performed in air at 760, 850, 980, 1070 and 1100 °C, respectively.

The fracture surfaces of tensile ruptured specimens were examined by SUPRA 55 field emission scanning electron microscopy (FESEM). The ruptured specimens were then cut along the longitudinal sections which were parallel to the tensile axis, and the sections were also perpendicular to the [001] orientation of the grasp side of the tensile ruptured specimens, as shown in Fig. 3. The microstructures of the sections were observed by optical microscopy (OM) and FESEM. Samples for OM and SEM observation were polished and etched with a chemical etchant of 100 mL H_2O + 80 mL HCl + 25 g $CuSO_4$ + 5 mL H_2SO_4 for 5−10 s. The 0.4 mm thin foils for transmission electron microscopy (TEM) analysis were cut parallel to the stress axis and about 5 mm apart from the fracture surface. They were mechanically ground to 50 μm and finally electro-polished at −30 °C in a solution of 10% perchloric acid + 90% ethyl alcohol, and then they were observed on JEOL JEM−2100F TEM operating at 200 kV.

3 Results and discussion

3.1 Microstructures of specimens

Figure 4 illustrates the microstructures of the as-cast [100], [120] and [110] specimens. The dendrites are well-arranged, and the [100] orientations of the specimens are different from each other, while the [001] orientations are almost the same. Figure 5 shows the

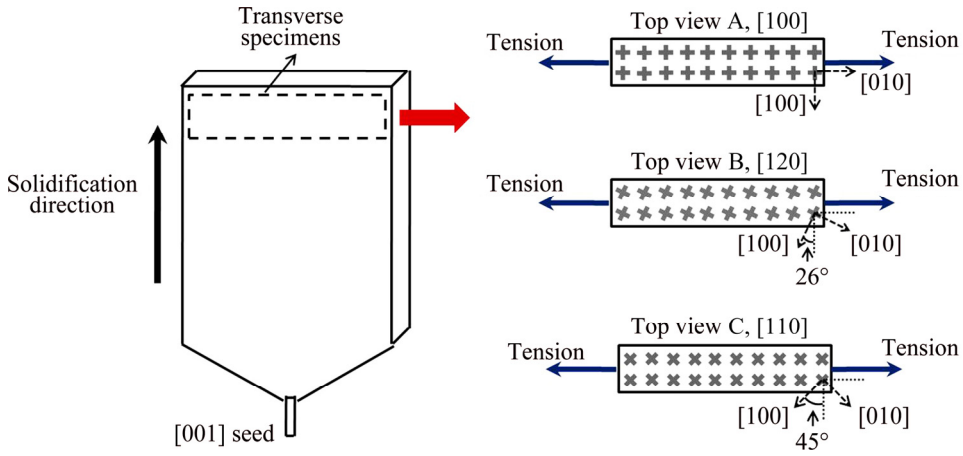

Fig. 1 Schematic of single crystal slab and transverse specimens

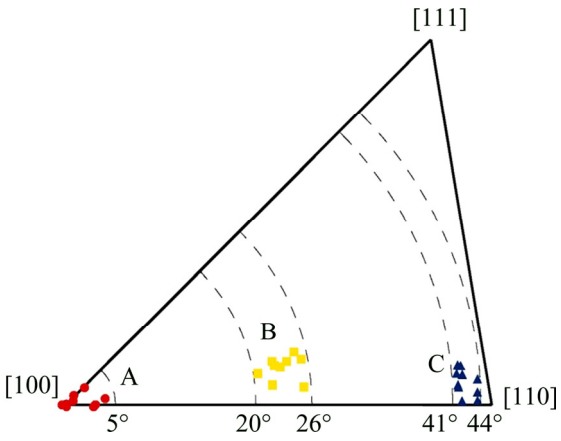

Fig. 2 Initial orientations of transverse specimens in [100] corner of standard stereographic triangle

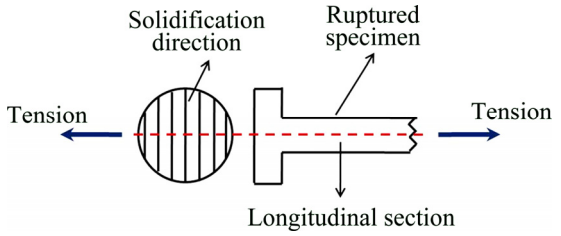

Fig. 3 Schematic diagram of longitudinal section of tensile ruptured specimen

microstructure of fully heat-treated specimens. It can be seen that the microstructures consist of γ phase and γ' phase. The γ' phases distribute uniformly in the γ matrix with an average size of about 0.4 μm, and the cuboidal form of them is well-developed.

3.2 Tensile properties

Figure 6 shows the elastic modulus of [100], [120] and [110] specimens at various temperatures, which is obtained from the tensile test. As can be seen, [100] specimens possess the lowest elastic modulus and the elastic modulus of [110] specimens is the highest. The elastic modulus of [100] specimens exhibits apparent decreasing with the increase of temperature, and the elastic modulus of [120] specimens decreases at firstly and then almost remains unchanged with the increase of temperature, while that of [110] specimens drops firstly and then increases a little as temperature increases. The atom arrangements along different orientations are different and the orientation dependence of the elastic modulus is similar in other single crystal superalloys [16,17].

The yield strength (YS) and ultimate tensile strength (UTS) of [100], [120] and [110] specimens at different temperatures are presented in Fig. 7. When the temperature is above 850 °C, the YS and UTS of all the

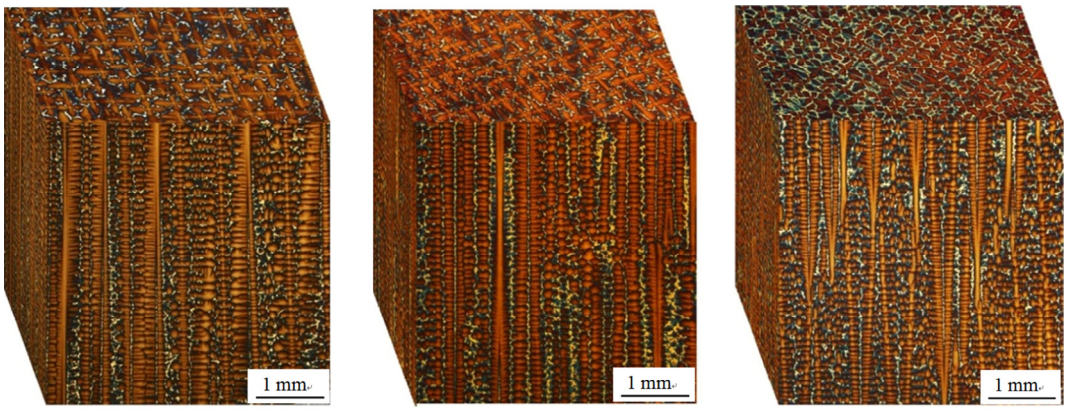

Fig. 4 OM images of dendrity morphologies of as-cast specimens: (a) [100] specimen; (b) [120] specimen; (c) [110] specimen

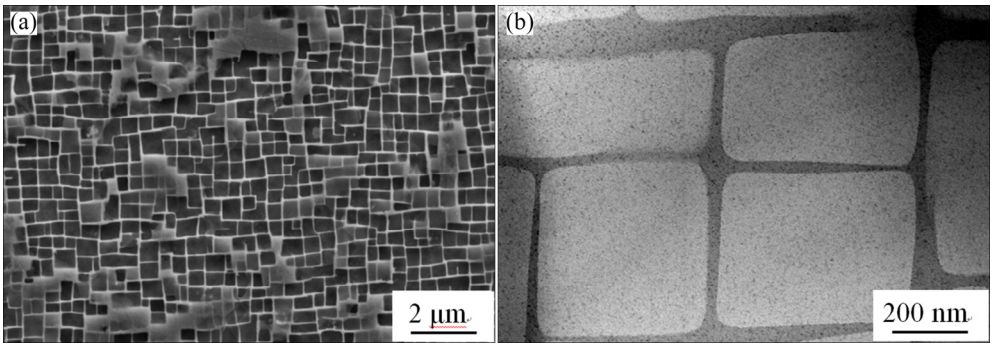

Fig. 5 Typical microstructures of specimens after heat treatment: (a) SEM; (b) TEM

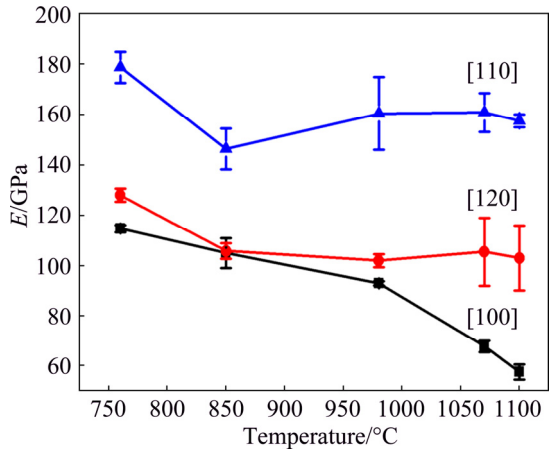

Fig. 6 Elastic modulus of [100], [120] and [110] specimens at different temperatures

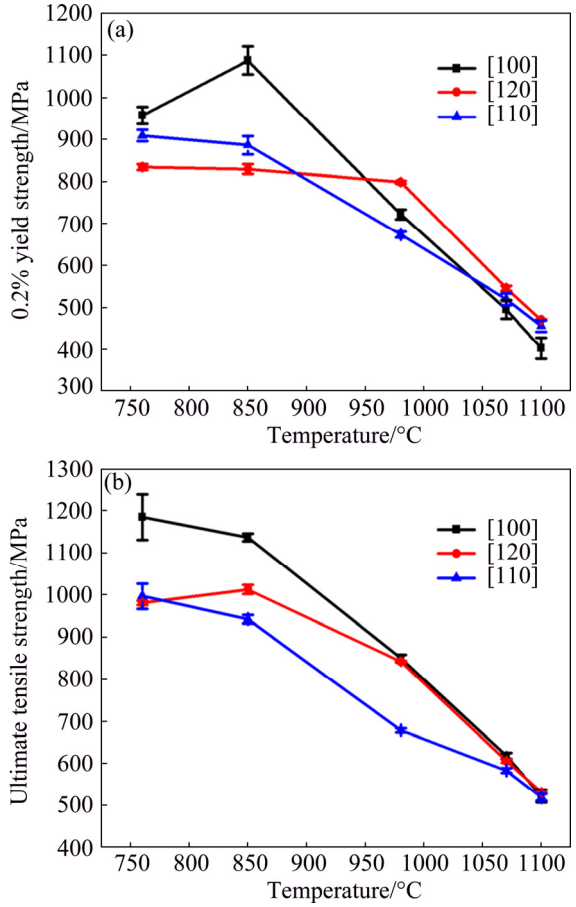

Fig. 7 Yield strength (a) and ultimate tensile strength (b) of [100], [120] and [110] specimens at different temperatures

specimens decrease monotonically with the rise of temperature. At 760 and 850 °C, the YS of [100] specimen is higher than that of [120] and [110] specimens, while at 980 °C the YS of [120] specimen is the highest. When the temperature is above 980 °C, there is little difference among the YS of all specimens. The UTS of [100] specimen is the highest from 760 to 980 °C, while the UTS of all specimens is almost the same at 1070 and 1100 °C. In general, the tensile strength of [100] specimen is higher than that of [120] and [110] specimens at 760 and 850 °C; while as the temperature is higher than 980 °C, the tensile strength of these three types of specimens has little difference.

Stress−strain curves at 760 and 1100 °C are shown in Fig. 8. At 760 °C, all specimens exhibit an apparent strain-hardening effect. [100] specimen does not show a well-defined yield point, while [120] and [110] specimens do. After the yield point, the flow stress of [100] specimen increases immediately; however, the flow stress of [120] specimen remains stable firstly and then increases, and the flow stress of [110] specimen drops a little to a serrated stage and then increases gradually. All three flow stress curves almost become a flat platform before rupture. At 1100 °C, the flow stress of all the specimens does not show a significant strain-hardening effect, and they all own a double-stage feature. In the second stage of the curve, the stress increases dramatically to the peak point and then drops gradually until rupture.

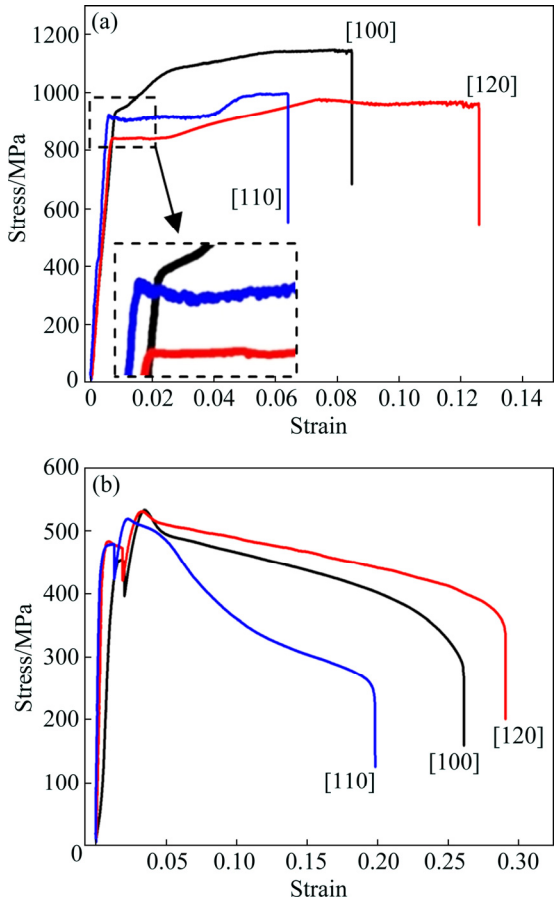

Fig. 8 Stress−strain curves of [100], [120] and [110] specimens at different temperatures: (a) 760 °C; (b) 1100 °C

3.3 Tensile fracture

Figures 9−11 show the tensile fracture surfaces and longitudinal photographs of [100], [120] and [110]

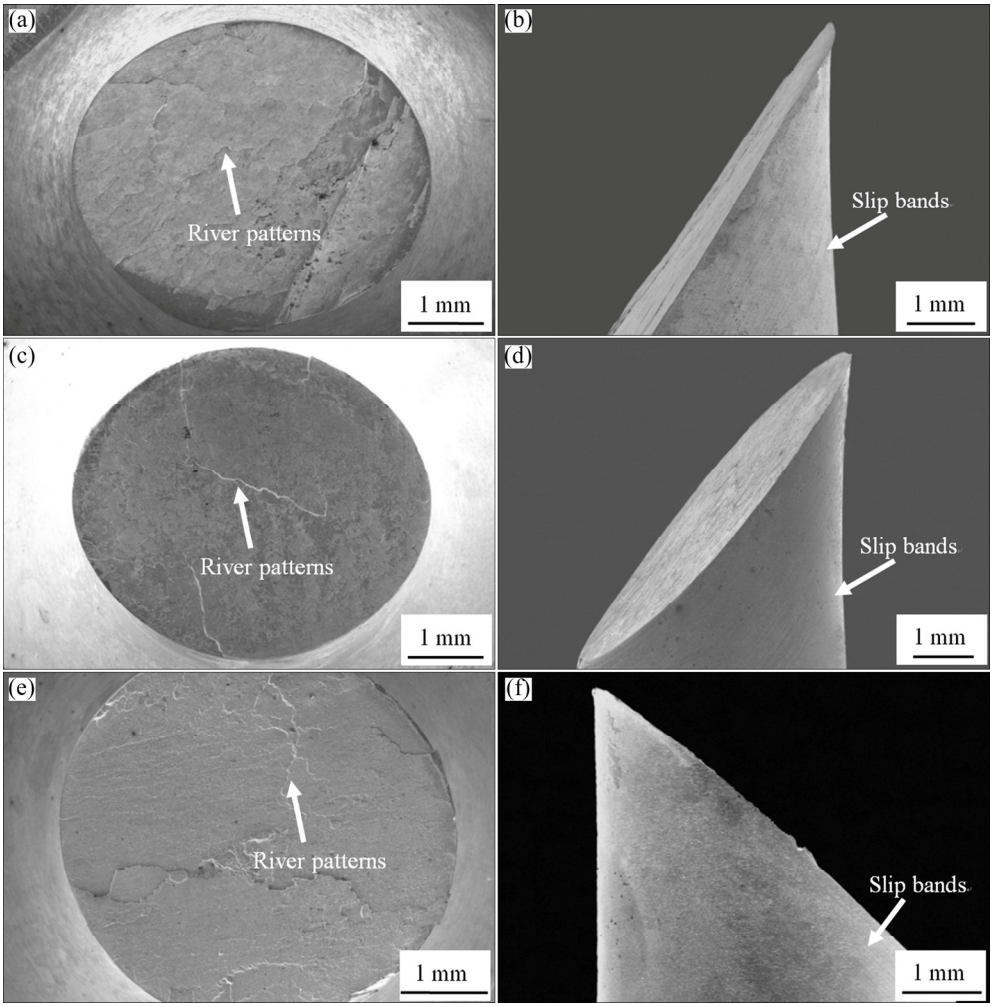

Fig. 9 Tensile fracture surfaces and longitudinal morphologies of specimens at 760 °C: (a, b) [100] specimen; (c, d) [120] specimen; (e, f) [110] specimen

specimens at 760, 980 °C and 1100 °C. At 760 °C, the fracture surfaces of all the specimens are similar. The fracture surfaces are almost circular, and there are river patterns on the fracture surfaces. The neck-down of the specimens is not obvious near the fracture surfaces. It can also be seen from Figs. 9(b, d, f) that there are slip bands parallel to the fracture surfaces. This means that the fracture occurs along the {111} plane, which is usually observed to be the cleavage plane in the tensile fracture of single crystal superalloys [18]. The fracture surfaces are all characterized by quasi-cleavage features, which is similar to other single crystal superalloys [10,11,14,15].

At 980 °C, the fracture surfaces of [100] and [120] specimens are almost circular, and there are facets on the fracture surfaces. At the same time, dimple features can be found on the other part of the fracture surfaces. Therefore, the fracture surfaces of [100] and [120] specimens display mixed quasi-cleavage and dimple features. There is slight neck-down of both [100] and [120] specimens near the fracture surfaces. As for [110] specimen, the fracture surface at 980 °C is composed of many small planes with tear ridges between them, and dimple features can also be observed on the fracture surface (Fig. 10(e)). Besides, it can be seen that there is an apparent neck-down of the specimen near the fracture surface (Fig. 10(f)). The fracture surface of [110] specimen shows both quasi-cleavage and dimple features.

At 1100 °C, the fracture surface of [100] specimen is circular and that of [120] specimen is a little elliptical, while that of [110] specimen is more elliptical. Meanwhile, a slight neck-down of [100] specimen can be observed near the fracture surface, and [120] specimen shows no obvious neck-down, while the fracture surface of [110] specimen exhibits a severe neck-down. There are dendrites characteristic and dimple features on the fracture surfaces of the [100] and [120] specimens, and the fracture surfaces of them are characterized by dimple features. However, the fracture surface of [110] specimen is apparently different from the other two types of specimens. Besides dimple features, single planes can

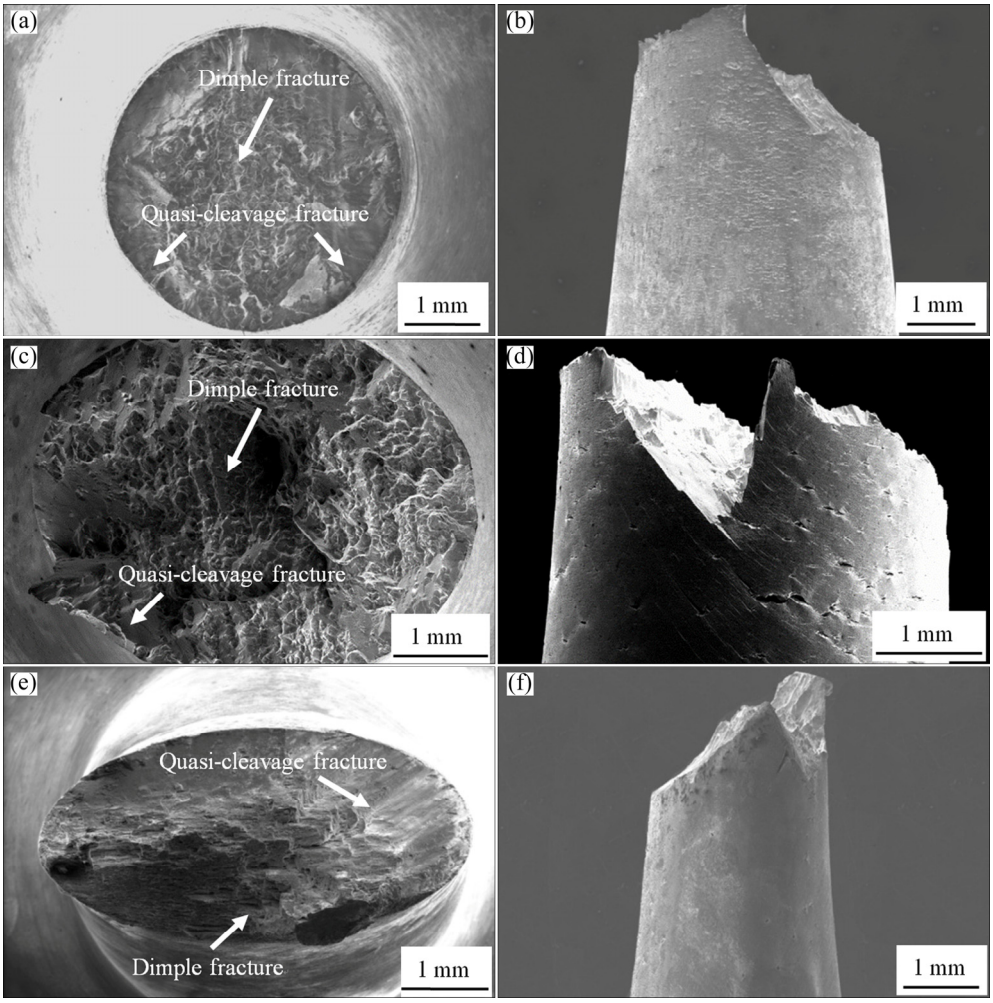

Fig. 10 Tensile fracture surfaces and longitudinal morphologies of specimens at 980 °C: (a, b) [100] specimen; (c, d) [120] specimen; (e, f) [110] specimen

also be observed on the fracture surface. Therefore, [110] specimen shows a mixed quasi-cleavage and dimple featured fracture surface at 1100 °C.

3.4 Microstructures of specimens after tensile rupture

Figure 12 shows morphologies of the longitudinal section of ruptured [100] specimens at 760, 980 and 1100 °C. It can be seen that no microcrack is found on the longitudinal section at 760 °C. However, microcracks can be observed inside the specimens as well as on the outer surfaces of the specimens at 980 and 1100 °C. It is also obvious that there are more microcracks on the longitudinal section at 1100 °C than at 980 °C. The above phenomenon of microcracks is similar for longitudinal sections of [120] and [110] specimens from 760 to 1100 °C.

Figure 13 illustrates the microstructures of the longitudinal sections near the fracture surfaces of ruptured [100], [120] and [110] specimens at 760, 980 and 1100 °C. At 760 °C, the γ' phases remain cubic and slip bands can be observed in all specimens. At 980 °C, the γ' phases remain cubic for all specimens. Two intersectional slip bands can be found near the fracture surface of [100] specimen, while there is only one kind of slip bands in [120] and [110] specimens. However, it is worthy to note that for [110] specimen, plenty of γ' phases get truncated by curved slip bands and the arrangement of γ' phases is affected near the fracture surface (Fig. 13(h)). At 1100 °C, shapes of the γ' phases in [100] and [120] specimens become irregular because the diffusion process is faster at the high temperature. The γ' phases are also slightly dissolved and the γ matrix channels become broadened under the tension load. For [110] specimen, the γ' phases in the highly deformed regions get elongated along the direction of the external stress, while the γ' phases in the undeformed regions are still relatively cubic (Fig. 13(i)).

Figure 14 shows the dislocation configurations of the longitudinal sections near the fracture surfaces of ruptured [100], [120] and [110] specimens at 760 °C. It can be seen that there are dislocations distributing parallel with each other in the γ matrix channels for all

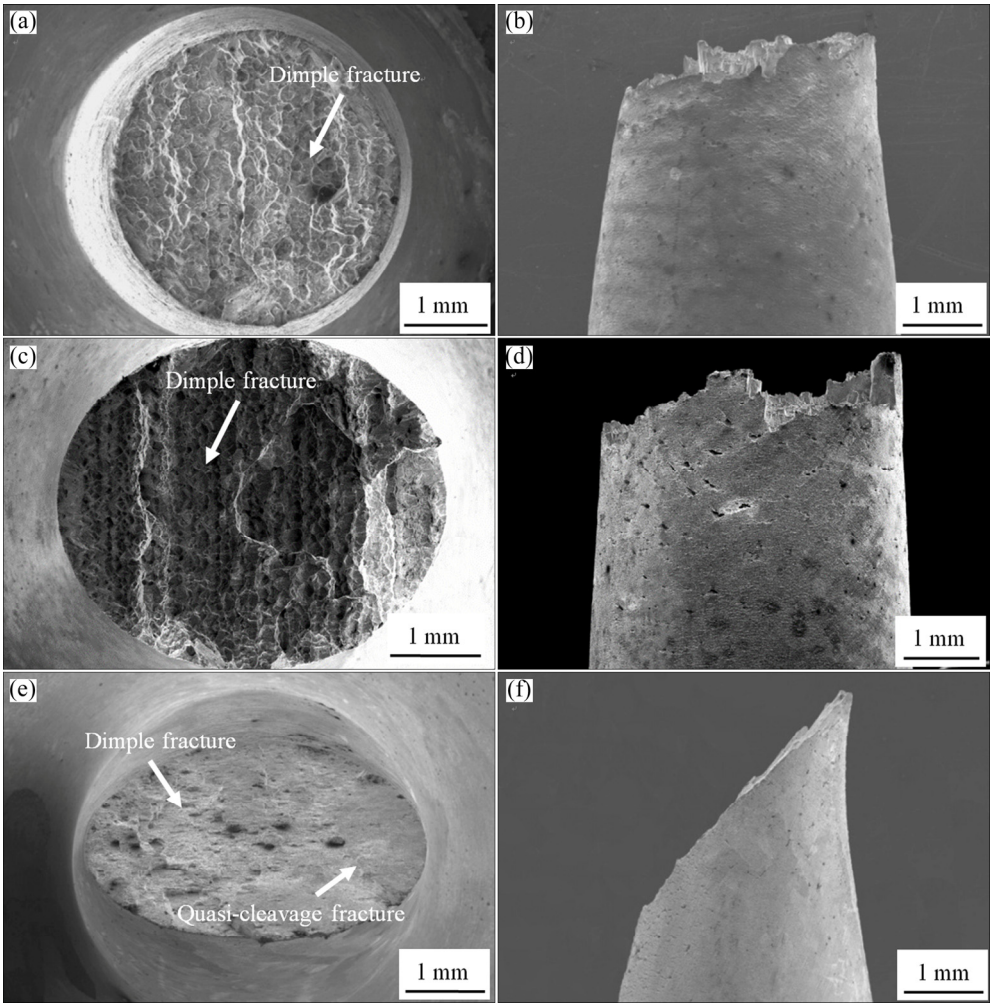

Fig. 11 Tensile fracture surfaces and longitudinal morphologies of specimens at 1100 °C: (a, b) [100] specimen; (c, d) [120] specimen; (e, f) [110] specimen

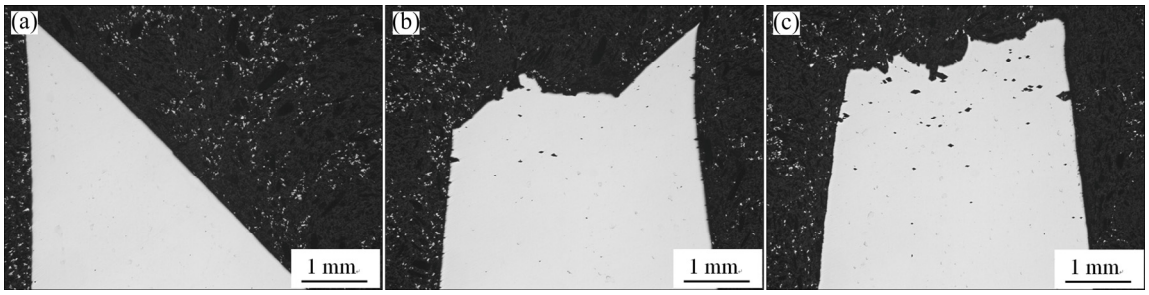

Fig. 12 Morphologies of longitudinal section of ruptured [100] specimens at different temperatures: (a) 760 °C; (b) 980 °C; (c) 1100 °C

specimens. This indicates that the deformation mechanism of the alloy at 760 °C is mainly the single slip. Besides, the superlattice stacking faults (SSFs) are obviously observed to transverse the whole γ' particles in [100] specimen, as indicated by arrows in Fig. 14(a), which is similar to the dislocation configuration of DD9 alloy with [001] orientation [11]. However, no obvious SSFs are found in [120] and [110] specimens. The SSFs are usually formed by the dissociation of γ/γ' interfacial $a/2\langle 110\rangle$ matrix dislocation via reaction $a/2\ [\bar{1}01] \rightarrow a/3[\bar{2}11]$ + SSF + $a/6[\bar{1}12]$, the $a/3\langle 112\rangle$ superpartial dislocation enters the γ' phase that creates an SSF, while the $a/6\langle 112\rangle$ partial dislocation remains at γ/γ' interface [19,20].

Figure 15 shows the dislocation configurations of the longitudinal sections near the fracture surfaces of ruptured [100], [120] and [110] specimens at 1100 °C. The dislocation configurations of all specimens at 1100 °C are similar. It can be observed that the dislocations are tangled and dislocation networks form.

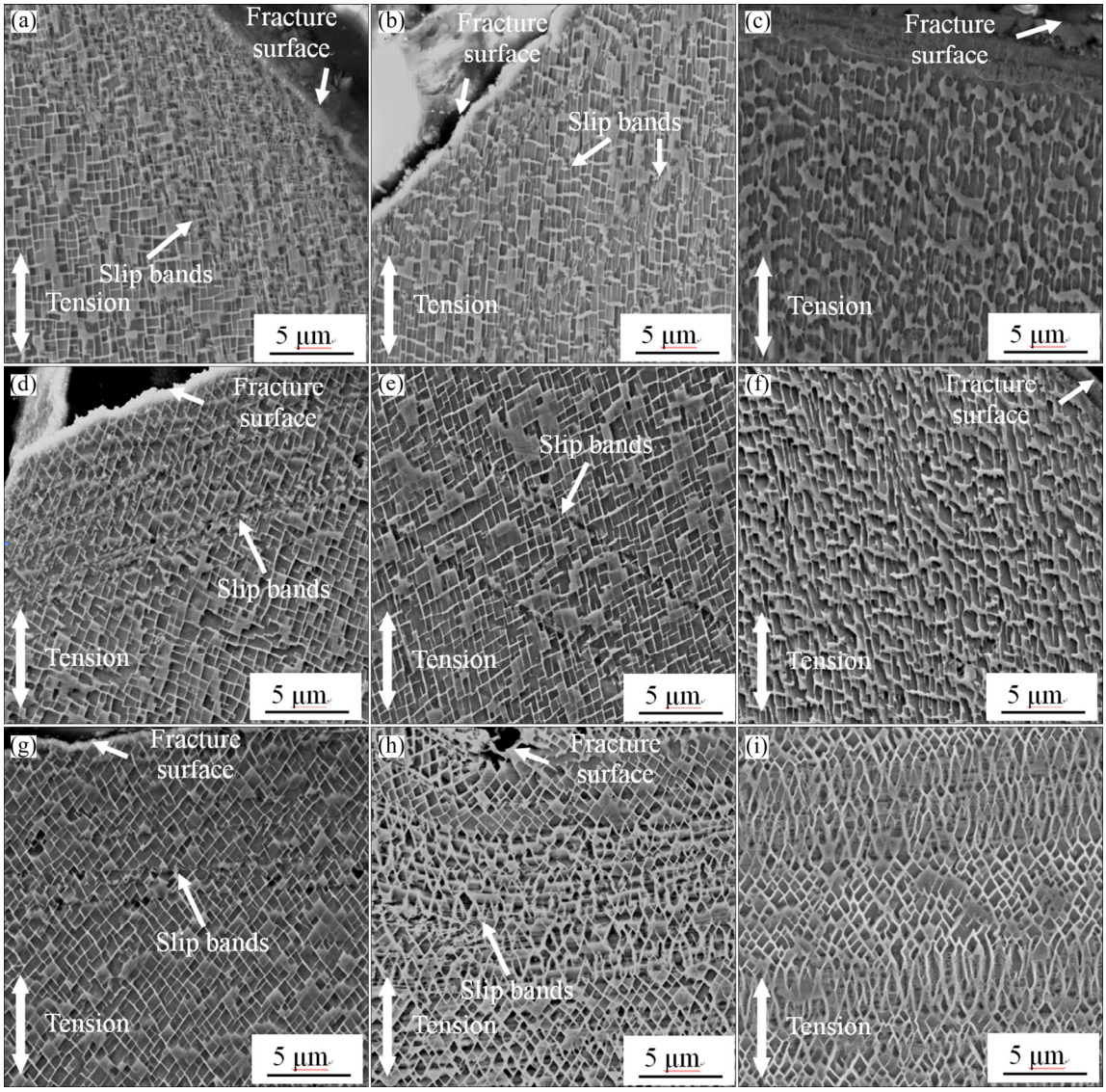

Fig. 13 Microstructures of longitudinal sections near fracture surfaces of ruptured [100], [120] and [110] specimens at different temperatures: (a) 760 °C, [100] specimen; (b) 980 °C, [100] specimen; (c) 1100 °C, [100] specimen; (d) 760 °C, [120] specimen; (e) 980 °C, [120] specimen; (f) 1100 °C, [120] specimen; (g) 760 °C, [110] specimen; (h) 980 °C, [110] specimen; (i) 1100 °C, [110] specimen

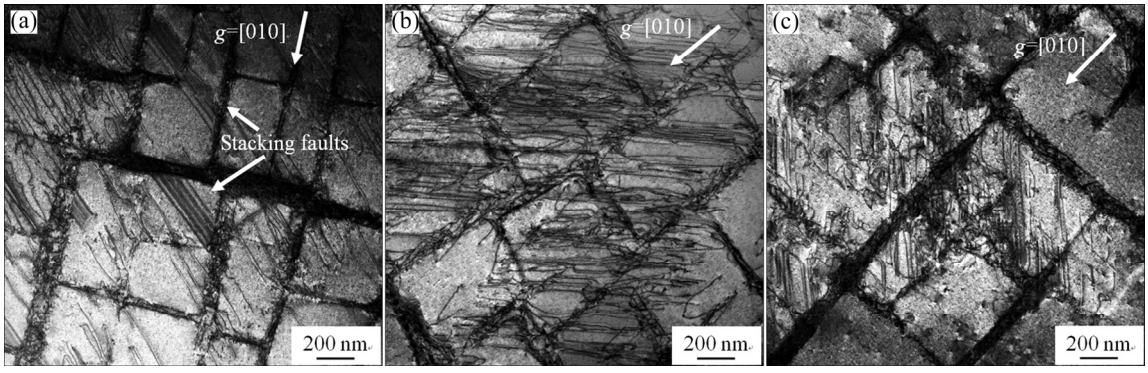

Fig. 14 Dislocation configurations near fracture surfaces of ruptured [100] (a), [120] (b) and [110] (c) specimens at 760 °C

Meanwhile, the shapes of the γ' phases become irregular, which is consistent with the result of the SEM (Fig. 13). These results indicate the occurrence of multiple slips and the reaction between different slip systems is strong. The activation of more slip systems at high temperatures results in dislocations intersection between different slip

systems, then the dislocations tangle and dislocation networks form, and they can act as barriers to dislocation movement through the γ' phases [21,22].

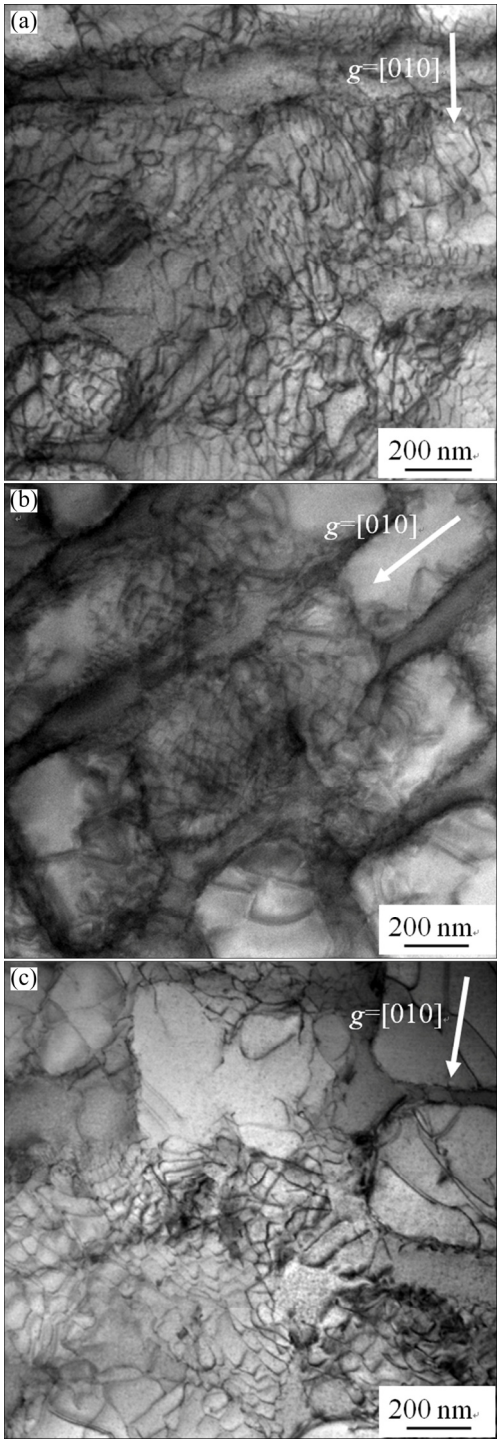

Fig. 15 Dislocation configurations near fracture surfaces of ruptured [100] (a), [120] (b) and [110] (c) specimens at 1100 °C

3.5 Correlation of microstructure and tensile behavior

The results above show that the tensile deformation behaviors of [100], [120] and [110] specimens are not the same, which means that the transverse tensile properties are anisotropic. However, the tensile anisotropy becomes weaker as the temperature increases.

3.5.1 Medium temperatures

At relatively low temperatures, the diffusion rates of the elements are low and the activity of the atoms is weak, and the activated slip systems are limited. It is shown that the slip system of the alloy at 760 °C is mainly {111}⟨110⟩. The fracture surface is characterized by quasi-cleavage feature at 760 °C. It can be seen from Figs. 9(b, d, f) that the normal directions of the fracture surface to the stress direction of [100], [120] and [110] specimens are about 57°, 49° and 40°, respectively. However, the angles between the {111}⟨110⟩ slip systems and the externally applied stress axis of [100], [120] and [110] specimens are theoretically calculated to be about 54.7°, 39.2° and 35.3°, respectively, which are smaller than the results in this study. This may because there are misorientation angles between the [001] orientation of the specimens and the longitudinal direction. Thus, the [001] orientation of the specimens is not completely perpendicular to the externally applied stress axis.

There are twelve octahedral {111}⟨110⟩ slip systems, and the Schmid factors of {111}⟨110⟩ slip system in [100] and [110] specimens are the same (0.41). However, when the external stress is parallel to [100] direction, the number of potential active slip systems is eight and there are only four potential active slip systems in [110] specimen as the external stress is parallel to [110] direction [17,23]. As for [120] specimen, the number of potential active {111}⟨110⟩ slip systems is twelve. However, only $(111)[0\bar{1}1]$ and $(\bar{1}\bar{1}1)[011]$ slip systems have the maximum Schmid factor (0.49), and six of other {111}⟨110⟩ slip systems have the Schmid factor of 0.24. Therefore, [120] specimen has the largest Schmid factor among [100], [120] and [110] specimens, and [120] specimen exhibits lower yield strength and higher elongation at 760 °C, as seen in Fig. 7(a) and Fig. 8(a). This is consistent with the result of other single crystal superalloy [24].

Besides, it is well accepted that the deformation mechanism at intermediate temperature is the γ' phase cut by $a/2\langle 110\rangle$ dislocation on octahedral slip systems [25]. The presence of SSFs in γ' phase is the result of the reaction of dislocation and γ' phase, and the SSFs can act as resistance to dislocation movement. After being tensile-ruptured at 760 °C, SSFs are obviously found in [100] specimen; however, no obvious SSFs are found in [120] and [110] specimens, as shown in Fig. 14. This may be a result of more slip systems operated in [100] specimen, thus making dislocation cutting γ' phase more easily. Therefore, [100] specimen does not possess a well-defined yield point and the flow

stress increases after yield (Fig. 8(a)). However, the serration part after the yield point of the flow stress of [110] specimen (Fig. 8(a)) may be as well related to less slip systems activated. Similar phenomenon has also been reported in René N4 alloy [9].

3.5.2 Elevated temperatures

As the temperature becomes higher, the activation energy to initiate the slip systems becomes lower and more slip systems are activated, including the octahedral {111}⟨110⟩ slip systems and the cubic {001}⟨110⟩ slip systems [26]. Thus, the tensile anisotropy is weak as the temperature is higher than 980 °C. However, the fracture surfaces of [110] specimens at high temperatures are apparently different from those of [100] and [120] specimens. The fracture surfaces of the latter at higher temperatures are mainly characterized by dimple features, just as [001] orientation single crystal superalloys exhibit [10,11,14], and the neck-down near the fracture surfaces is not obvious. For [110] specimens, there are fewer dimple features on the fracture surfaces and an apparent neck-down near the fracture surfaces can be observed. The fracture surfaces show an obvious shape change from cylindrical to elliptical during tensile tests. Considering the microstructures of the longitudinal sections near the fracture surface of [110] specimen, many γ' phases get truncated by curved slip bands at 980 °C (Fig. 13(h)), and the γ' phases in highly deformed regions get elongated while the γ' phases in the undeformed regions remain in relatively cubic morphology at 1100 °C (Fig. 13(i)).

Among [100], [120] and [110] specimens, the Schmid factor of {100}⟨110⟩ slip system in [110] specimen is the largest (0.35) and there are four potential active slip systems, which are (100)[011], (100)$[0\bar{1}1]$, (010)[101] and (010)$[\bar{1}01]$. However, the angles of the normal direction of the fracture surface to the stress direction in [110] specimens at 980 and 1100 °C are about 38° and 46°, respectively, as seen in Fig. 10(f) and Fig. 11(f). This implies that the {111}⟨110⟩ slip systems are dominant in [110] specimens at high temperatures. Therefore, the potential slip systems of [110] specimen are limited compared to those of [100] and [120] specimens, and [110] specimen has to twist itself to initiate more slip systems during the tensile test. As a result, the fracture surfaces of [110] specimen exhibit distinct elliptical shape. The elliptically shaped fracture surface has also been observed after tensile rupture of the SRR99 alloy, and it has been associated with crystal lattice rotation during the plastic deformation [17], which is consistent with the results in this study.

4 Conclusions

(1) The tensile strength of [100] specimen is higher than that of [120] and [110] specimens at 760 °C and 850 °C; while as the temperature is higher than 980 °C, the tensile strength of all the specimens has little difference.

(2) The fracture surfaces of [100], [120] and [110] specimens are characterized by quasi-cleavage features at 760 °C, while they all display mixed quasi-cleavage and dimple features at 980 °C. At 1100 °C, the fracture surfaces of [100] and [120] specimens are characterized by dimple features, while [110] specimen shows mixed quasi-cleavage and dimple featured fracture surfaces.

(3) At 760 °C, high densities of parallel dislocations are found to distribute in the γ matrix channels of [100], [120] and [110] specimens, and obvious SSFs are observed to remain in γ' particles in [100] specimen. At 1100 °C, the dislocation configurations of all specimens are similar, the dislocations are tangled and dislocation networks form as a result of the activation of more slip systems.

(4) The difference in the number of potential active slip systems in [100], [120] and [110] specimens during the tensile deformation process is the main reason for the transverse tensile anisotropy.

References

[1] GELL M, DUHL D N, GIAMEI A F. The development of single crystal superalloy turbine blades [C]//Proc Superalloy 1980. Warrendale, PA: TMS, 1980: 205−214.

[2] LI J R, LIU S Z, WANG X G, SHI Z X, ZHAO J Q. Development of a low-cost third generation single crystal superalloy DD9 [C]//HARDY M, HURON E, GLATZEL U, GRIFFIN B, LEWIS B, RAE C, SEETHARAMAN V, TIN S. Proc Superalloy 2016. Warrendale, PA: TMS, 2016: 57−63.

[3] SHI Zhen-xue, LIU Shi-zhong, WANG Xiao-guang, LI Jia-rong. Effects of Cr content on microstructure and mechanical properties of single crystal superalloy [J]. Transactions of Nonferrous Metals Society of China, 2015, 25(3): 776−782.

[4] ARAKERE N K, SWANSON G. Effect of crystal orientation on fatigue failure of single crystal nickel base turbine blade superalloys [J]. Journal of Engineering for Gas Turbines and Power, 2002, 124: 161−176.

[5] SENGUPTA A, PUTATUNDA S K, BARTOSIEWICZ L, HANGAS J, NAILOS P J, PEPUTAPECK M, ALBERTS F E. Tensile behavior of a new single-crystal nickel-based superalloy (CMSX-4) at room and elevated temperatures [J]. Journal of Materials Engineering and Performance, 1994, 3: 73−81.

[6] ZHANG Peng, YUAN Yong, LI Bo, YANG Gong-xian, SONG Xiao-long. Investigation of tensile deformation mechanisms at room temperature in a new Ni-based single crystal superalloy [J]. Philosophical Magazine Letters, 2016, 96: 238−245.

[7] ZHAO Yun-xing, WANG Xin, LIU Jun, HUANG Lan, JIANG Liang. Microstructure and mechanical properties of new nickel-base single crystal superalloy [J]. The Chinese Journal of Nonferrous Metals, 2015, 25: 2695−2706. (in Chinese)

[8] SHAH D M, DUHL D N. The effect of orientation, temperature and gamma prime size on the yield strength of a single crystal nickel base superalloy [C]//Proc Superalloy 1984. Warrendale, PA: TMS, 1984: 105−114.

[9] MINER R V, VOIGT R C, GAYDA J, GABB T P. Orientation and temperature dependence of some mechanical properties of the single-crystal nickel-base superalloy René N4: Part I. Tensile behavior [J]. Metallurgical Transactions A, 1986, 17: 491−496.
[10] LI Jia-rong, SHI Zhen-xue, YUAN Hai-long, LIU Shi-zhong, ZHAO Jin-qian, HAN Mei, LIU Wei-wei. Tensile anisotropy of single crystal superalloy DD6 [J]. Journal of Materials Engineering, 2008, 12: 6−10. (in Chinese)
[11] WANG Xiao-guang, LI Jia-rong, YU Jian, LIU Shi-zhong, SHI Zhen-xue, YUE Xiao-dai. Tensile anisotropy of single crystal superalloy DD9 [J]. Acta Metallurgica Sinica, 2015, 51: 1253−1260. (in Chinese)
[12] SABNIS P A, MAZIÈRE M, FOREST S, ARAKERE N K, EBRAHIMI F. Effect of secondary orientation on notch-tip plasticity in superalloy single crystals [J]. International Journal of Plasticity, 2012, 28: 102−123.
[13] ZHOU Z J, WANG L, WANG D, LOU L H, ZHANG J. Effect of secondary orientation on room temperature tensile behaviors of Ni-base single crystal superalloys [J]. Materials Science and Engineering A, 2016, 659: 130−142.
[14] ZHAO Jin-qian, LI Jia-rong, LIU Shi-zhong, HAN Mei. Transverse tensile properties of second generation single crystal superalloy DD6 [J]. Journal of Materials Engineering, 2007, 12: 12−20. (in Chinese)
[15] SHI Zhen-xue, LI Jia-rong, LIU Shi-zhong, ZHAO Jin-qian. Transverse tensile properties and fracture behaviour of DD6 single crystal superalloy [J]. Journal of Aeronautical Materials, 2009, 29: 101−104. (in Chinese)
[16] DYE D, COAKLEY J, VORONTSOV V A, STONE H J, ROGGE R B. Elastic moduli and load partitioning in a single-crystal nickel superalloy [J]. Scripta Materialia, 2009, 61: 109−112.
[17] WANG L N, LIU Y, YU J J, XU Y, SUN X F, GUAN H R, HU Z Q, Orientation and temperature dependence of yielding and deformation behavior of a nickel-base single crystal superalloy [J]. Materials Science and Engineering A, 2009, 505: 144−150.
[18] EBRAHIMI F, YANEVICH J, DELUCA D P. Deformation and fracture of the PWA 1472 superalloy single crystal [J]. Acta Materialia, 2000, 48: 469−479.
[19] LIU Jin-lai, YU Jin-jiang, JIN Tao, SUN Xiao-feng, GUAN Heng-rong, HU Zhuang-qi. Influence of temperature on tensile behavior and deformation mechanism of Re-containing single crystal superalloy [J]. Transactions of Nonferrous Metals Society of China, 2011, 21(7): 1518−1523.
[20] MILLIGAN W W, ANTOLOVICH S D. Yielding and deformation behavior of the single crystal superalloy PWA 1480 [J]. Metallurgical Transactions A, 1987, 18: 85−95.
[21] FELLER-KNIEPMEIER M, LINK T, POSCHMANN I, SCHEUNEMANN-FRERKER G, SCHULZE C. Temperature dependence of deformation mechanisms in a single crystal nickel-base alloy with high volume fraction of γ′ phase [J]. Acta Materialia, 1996, 44: 2397−2407.
[22] ZHANG Xuan, JIN Tao, ZHAO Nai-ren, WANG Zhi-hui, SUN Xiao-feng, GUAN Heng-rong, HU Zhuang-qi. Temperature dependence of deformation mechanism in single crystal Ni-base superalloy [J]. Transactions of Nonferrous Metals Society of China, 2005, 15(4): 759−763.
[23] SASS V, GLATZEL U, FELLER-KNIEPMEIER M. Creep anisotropy in the monocrystalline nickel-base superalloy CMSX-4 [C]//KISSINGER R D, DEYE D J, ANTON D L, CETEL A D, NATHAL M V, POLLOCK T M, WOODFORD D A. Proc Superalloy 1996. Warrendale, PA: TMS, 1996: 283−290.
[24] MACKAY R A, DRESHFIELD R L, MAIER R D. Anisotropy of nicakel-base superalloy single crystals [C]//Proc Superalloy 1980. Warrendale, PA: TMS, 1980: 385−394.
[25] SCHEUNEMANN-FRERKER G, GABRISCH H, FELLER-KNIEPMEIER M. Dislocation microstructure in a single-crystal nickel-based superalloy after tensile testing at 823 K in the [001] direction [J]. Philosophical Magazine A, 1992, 65: 1353−1368.
[26] TAMAKI H, FUJITA K, OKAYAMA A, MATSUDA N, YOSHINARI A, KAKEHI K. A study on bending deformation behavior of Ni-based DS and SC superalloys [C]//GREEN K A, POLLOCK T M, HARADA H, HOWSON T E, REED R C, SCHIRRA J J, WALSTON S. Proc Superalloy 2004. Warrendale, PA: TMS, 2004: 145−154.

取向偏离度对镍基第三代单晶高温合金 DD9 在 760~1100 °C 横向拉伸性能的影响

杨万鹏，李嘉荣，刘世忠，史振学，赵金乾，王效光

北京航空材料研究院 先进高温结构材料重点实验室，北京 100095

摘　要：研究[100]、[120]和[110]取向的镍基第三代单晶高温合金 DD9 在 760~1100 °C 范围内的拉伸性能。采用 OM、SEM 和 TEM 观察显微组织与断口形貌。结果表明，[100]取向试样在 760 °C 和 850 °C 的抗拉强度高于[210]和[110]取向试样，而在 980 °C 以上，三种取向试样的抗拉强度接近。[100]、[120]和[110]取向试样在 760 °C 与 980 °C 的断裂机制相同，而在 1100 °C 条件下，[100]与[120]取向试样断口为韧窝断裂，而[110]取向试样断口为类解理断裂与韧窝断裂共存。在 760 °C 条件下，仅在[100]取向试样中发现明显层错，而在 1100 °C 条件下三种取向试样中位错组态相似。[100]、[120]和[110]取向试样拉伸变形过程中可开动的潜在滑移系数量不同是造成横向拉伸性能各向异性的主要原因。

关键词：第三代单晶高温合金；DD9；横向拉伸性能；各向异性；断口

(Edited by Bing YANG)